

Article

Freeze-Drying-Assisted Preparation of High-Compaction-Density $\text{LiMn}_{0.69}\text{Co}_{0.01}\text{Fe}_{0.3}\text{PO}_4$ Cathode Materials with High-Capacity and Long Life-Cycle for Lithium Ion Batteries

Shaojun Liu ^{1,†}, Jingang Zheng ^{1,†}, Hao Huang ¹, Hongyang Li ¹, Han Zhang ¹ , Lixiang Li ¹, Baigang An ¹, Yuanhua Xiao ^{2,*} and Chengguo Sun ^{1,3,*} 

¹ School of Chemical Engineering, University of Science and Technology Liaoning, Anshan 114051, China; sjliu@home.ipe.ac.cn (S.L.); zjg1764124@163.com (J.Z.); hhao2000@126.com (H.H.); hnjzlh@126.com (H.L.); hzhang0807@163.com (H.Z.); lxli2005@126.com (L.L.); bgan@ustl.edu.cn (B.A.)

² State Laboratory of Surface and Interface Science and Technology, College of Materials and Chemical Engineering, Zhengzhou University of Light Industry, Zhengzhou 450002, China

³ School of Chemical Engineering, Nanjing University of Science and Technology, Nanjing 210094, China

* Correspondence: yuanhua_xiao@zzuli.edu.cn (Y.X.); sunyangguo2004@163.com (C.S.)

† These authors contributed equally to this work.

Abstract: As a successor to LiFePO_4 , the research interest in $\text{LiMn}_{1-y}\text{Fe}_y\text{PO}_4$ has been sustained due to its higher working voltage and safety features. However, its further application is limited by the low compaction density caused by uncontrolled particle size. In this study, the high-quality $\text{LiMn}_{0.69}\text{Co}_{0.01}\text{Fe}_{0.3}\text{PO}_4$ (LMFP) materials were prepared using the freeze-drying method to process the LMFP precursor synthesized through a solvothermal crystallization method followed by a calcination process at different temperatures (400–550 °C). The results demonstrate that the obtained particles exhibit a spheroidal shape with a low specific surface area after secondary crystallization calcination at 700 °C. The compaction density increased from 1.96 g/cm³ for LMFP precursor (LMFP-M1) to 2.18, 2.27, 2.34, and 2.43 g/cm³ for samples calcined at 400, 450, 500 and 550 °C, respectively, achieving a maximum increase of 24%. The full cell constructed with the high-compaction-density material calcined at 500 °C displayed discharge capacities of 144.1, 143.8, and 142.6 mAh/g at 0.5, 1, and 3 C rates, respectively, with a retention rate of 99% at 3 C rate. After undergoing charging and discharging cycles at a rate of 1 C for up to 800 cycles, the capacity retention rate was found to be 90%, indicating an expected full cell life span exceeding 2500 cycles.

Keywords: $\text{LiMn}_{1-y}\text{Fe}_y\text{PO}_4$; high-compaction density; high energy density; secondary crystallization



Citation: Liu, S.; Zheng, J.; Huang, H.; Li, H.; Zhang, H.; Li, L.; An, B.; Xiao, Y.; Sun, C. Freeze-Drying-Assisted Preparation of High-Compaction-Density $\text{LiMn}_{0.69}\text{Co}_{0.01}\text{Fe}_{0.3}\text{PO}_4$ Cathode Materials with High-Capacity and Long Life-Cycle for Lithium Ion Batteries. *Batteries* **2024**, *10*, 114. <https://doi.org/10.3390/batteries10040114>

Academic Editor: Carlos Ziebert

Received: 2 February 2024

Revised: 1 March 2024

Accepted: 12 March 2024

Published: 25 March 2024



Copyright: © 2024 by the authors. Licensee MDPI, Basel, Switzerland. This article is an open access article distributed under the terms and conditions of the Creative Commons Attribution (CC BY) license (<https://creativecommons.org/licenses/by/4.0/>).

1. Introduction

Over the past two decades, olivine LiFePO_4 has emerged as a prominent cathode material for lithium ion batteries (LIBs), especially in applications such as electric vehicles and large-scale energy storage systems, owing to its notable safety profile, minimal environmental impact, and affordability [1–5]. In particular, for the year of 2023, among the three mainstream power batteries (LiFePO_4 , LiNiCoMnO_2 , and LiMnO_2), 67.3% of the power batteries installed in domestic new energy vehicles were LiFePO_4 batteries, based on the data reported by the China Automotive Battery Innovation Alliance. As for the high demand for electric vehicle cruise range per charge, further boosting the energy density of LiFePO_4 batteries suffers from the limitation of available battery assembly technology and lower operating potential (3.4 V vs. Li/Li^+), as well as the theoretical capacity of 170 mAh/g (578 Wh kg⁻¹) [6–8]. In view of the highly stable olivine framework, one way to increase the energy density is the replacement of Fe by Mn to form LiMnPO_4 or $\text{LiMn}_{1-y}\text{Fe}_y\text{PO}_4$. As shown in Figure 1a, the substituted benefit is that the working voltage of LiMnPO_4 can be increased to about 4.1 V (vs. Li/Li^+), the theoretical energy density

is 21% higher than LiFePO_4 , equal to $\text{LiNi}_{0.5}\text{Co}_{0.2}\text{Mn}_{0.3}\text{O}_2$, and up to 700 Wh kg^{-1} [9–12]. Although $\text{LiMn}_{1-y}\text{Fe}_y\text{PO}_4$ does not reach the high theoretical energy density of sulfur (2600 Wh kg^{-1} and 2800 Wh L^{-1}) [13,14], and the ultra-high theoretical specific energy of Li_2O_2 (3458 Wh kg^{-1}) [15], in the short term, $\text{LiMn}_{1-y}\text{Fe}_y\text{PO}_4$ is the most promising material to replace the three main materials in the existing commercialized power battery market due to its excellent overall performance.

Regrettably, LiMnPO_4 exhibits lower electronic conductivity and lithium ion diffusivity in comparison to LiFePO_4 [16,17]. The substantial kinetic discrepancies between them originate from inherent characteristics, encompassing crystallographic features and transport properties [18]. A critical feature of the structure of LiMnPO_4 is the isolation of the Mn–O octahedron by the P–O tetrahedron, distinct from the continuous M–O network observed in LiMn_2O_4 . The robust covalent bonding within the P–O framework impedes Li^+ ions from traversing through the PO_4^{3-} tetrahedral sites, thereby directing Li^+ ion transport predominantly along the *b*-axis, following a one-dimensional diffusion pathway [12,19]. The deposition/stripping dynamics adhere to a biphasic principle, marked by a pronounced lattice disparity from the MnPO_4 to LiMnPO_4 phases. This divergence not just imposes a considerable energy impediment to the exchange of lithium ions at the interphase boundary but amplifies the energy requisite of electronic transitions [20–22]. The observed phenomena can be owed to the electronic–lattice interactions surrounding the ions of Mn^{3+} , where a pronounced Jahn–Teller effect significantly confines the polaron gap, thereby rapidly increasing the polaron’s effective mass. The augmented effective polaronic mass at the sites of Mn^{3+} , in conjunction with the substantial number of localized lattice distortions, leads to diminished kinetic rates and increased internal friction. This effect is manifested both within the body structure of a crystal as well as at the phase boundary of $\text{LiMnPO}_4/\text{MnPO}_4$, which is featured by lattice mismatch, potentially obstructing the one-dimensional lithium ion diffusion pathway [23–25]. Therefore, the optimistic perspectives for LiMnPO_4 as a practical cathode have not been widely accepted. Considering the advantages of LiFePO_4 and LiMnPO_4 , a compromise is that Mn is used to replace partial Fe ions from the olivine LiFePO_4 , thereby forming $\text{LiMn}_{1-y}\text{Fe}_y\text{PO}_4$ [26,27]. Subsequent to *ab initio* calculations, it has been determined that the substitution of Mn with Fe enhances the mutual solubility of $\text{LiMn}_{1-y}\text{Fe}_y\text{PO}_4$ and $\text{Mn}_{1-y}\text{Fe}_y\text{PO}_4$, leading to an enlargement of the single-phase region and a reduction in the two-phase region. The extent of the single-phase region is contingent upon the Fe/(Fe+Mn) ratio, with the broadest extent of solid solution observed when the ions of Fe substitution reach 15–30 mol% [20,28]. Although $\text{LiMn}_{1-y}\text{Fe}_y\text{PO}_4$ possesses the above-mentioned advantages, it still has some unsolved issues including particle size control, low compaction density, electron conductivity, ionic diffusion, and carbon coating technology [29–32] (Figure 1a,c). The low tap density limits its application in power batteries. However, the compaction density of the material is related to the primary particle size and the pores between the particles. Effectively increasing the primary particle size and reducing the pores between particles can significantly enhance the material’s compaction density [27]. In our previous research, we employed a solvothermal method to regulate the particle size of $\text{LiMn}_{1-y}\text{Fe}_y\text{PO}_4$, ensuring preferential growth along the (010) crystal planes through crystal orientation control techniques [33]. Furthermore, we modified the LMFP material through Co doping and carbon coating techniques. The results not only significantly enhanced the kinetic properties but also successfully increased the particle size, thereby improving the material’s compaction density. However, the prepared LMFP has limited potential in improving the material’s compaction density. The LMFP samples have elongated and rod-like particles with high aspect ratios, which tend to form larger voids during the stacking process, leading to a challenge in further compaction of the material even under high external forces [34,35]. In contrast, spherical LMFP particles exhibited higher tap density and significant improvements in flowability, dispersibility, and processability. These unique features are crucial for preparing high-quality cathode material slurries, optimizing electrode coating processes, and enhancing the overall performance of electrode sheets [36–38].

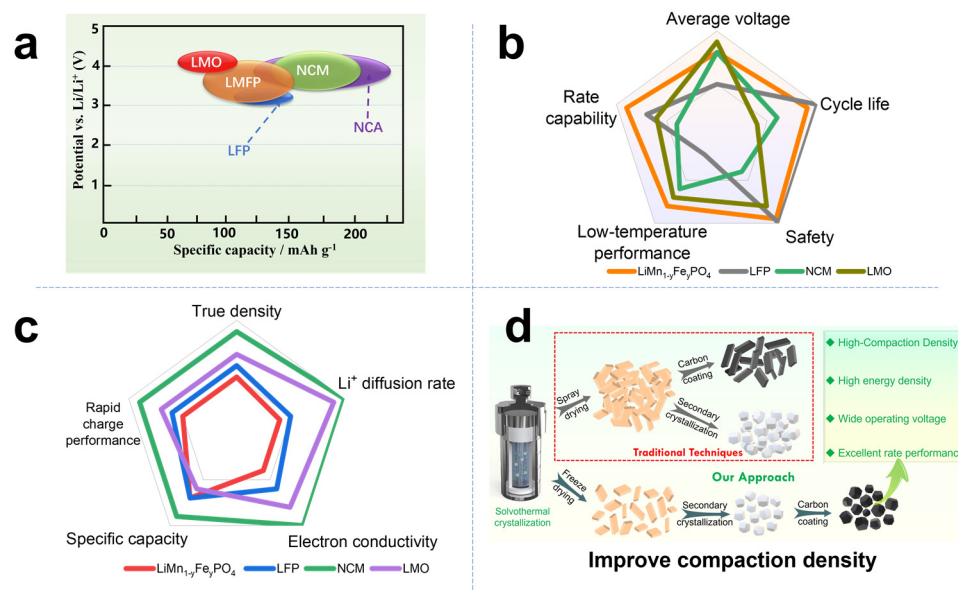


Figure 1. (a) The $\text{LiMn}_{1-y}\text{Fe}_y\text{PO}_4$ specific energy density taken from Refs. [8,12]; (b) Comprehensive performance taken from Refs. [8,29] and (c) electrochemical performance comparison radar chart of $\text{LiMn}_{1-y}\text{Fe}_y\text{PO}_4$, LFP, NCM and LMO taken from Refs. [20,30]; (d) the schematic diagram of the preparation process.

Herein, we have developed an innovative freeze-drying-assisted method to enhance the particle size and morphology of LMFP [32,39–41]. By precisely controlling the crystal growth process, our results demonstrate successful spherification of particles with reduced surface area and minimized gaps between smaller particles. This approach effectively improves material compaction density while maintaining its nanoscale single-crystal structure to preserve high dynamic properties, which is advantageous for achieving enhanced compaction density. Furthermore, a comprehensive evaluation of electrochemical performance confirms that our optimized LMFP cathode material exhibits superior charge–discharge cycling properties at high rates. Overall, this work presents an effective strategy for enhancing both energy density and cycling stability in LMFP cathode materials.

2. Materials and Methods

2.1. Materials and Synthesis

All raw materials used, including lithium hydroxide, ferrous sulfate, manganese chloride, cobalt sulfate, and phosphoric acid, were provided by Sinopharm Chemical Reagent Co., Ltd., Shanghai, China and were of analytical purity. The LMFP cathode material was synthesized using the solvothermal method and ethylene glycol served as the solvent. The molar ratios of $\text{LiOH}\cdot\text{H}_2\text{O}$, divalent metal salts ($\text{MnCl}_2\cdot 4\text{H}_2\text{O}$, $\text{CoSO}_4\cdot 7\text{H}_2\text{O}$, $\text{FeSO}_4\cdot 7\text{H}_2\text{O}$) and H_3PO_4 were established at 3:1(0.69:0.01:0.3):1. The detail procedures are as follows: 5.5 g $\text{MnCl}_2\cdot 4\text{H}_2\text{O}$, 0.12 g $\text{Co}(\text{NO}_3)_2\cdot 6\text{H}_2\text{O}$, 3.4 g $\text{FeSO}_4\cdot 7\text{H}_2\text{O}$, and ethylene glycol (a volume of 80 mL) were then mechanically stirred, forming solution A. A total of 5.1 g of $\text{LiOH}\cdot\text{H}_2\text{O}$ dissolves in 80 mL ethylene glycol, labelled as solution B. Then, adding 5.96 g of H_3PO_4 to solution B formed the mixed solution C. Gradually, solution C was added into solution A by stirring for 30 min, and then it was transferred into a 200 mL autoclave and heated at 180 °C for 8 h. Subsequently, the solution was allowed to cool to room temperature, and the sample was obtained afterwards with centrifugal filtration. The LMFP precursor powders (named LMFP-M1) were dried in a freeze dryer.

The LMFP-M1 powder, under argon protection, was placed in a tubular furnace. The temperature was increased gradually by 5 °C/min to maintain 400, 450, 500, and 550 °C, each for 4 h (the samples were named LMFP-400, LMFP-450, LMFP-500, and LMFP-550). Subsequently, 8% sucrose (by mass) was added to LMFP-M1, LMFP-400, LMFP-450, LMFP-

500, and LMFP-550, then ground and dried. The aforementioned mixtures were conveyed to a tubular furnace and subjected to heating under an argon atmosphere at a rate of 5 °C/min up to 700 °C, whereupon this temperature was maintained for a duration of 4 h. The samples were then naturally cooled to room temperature inside the furnace, resulting in carbon-coated LMFP black powder (named LMFP-M1/C, LMFP-400/C, LMFP-450/C, LMFP-500/C, and LMFP-550/C, respectively) (Figure 1d).

2.2. Characterization

Material characterization tests in this study were conducted on the AXS D8 Advance instrument from Bruker, employing Cu-K α radiation, with a λ of 1.5406 Å, and a scan angles from 10° to 90°. The Apreos model scanning electron microscope (Thermo Fisher Scientific, Waltham, MA, USA) was used to characterize the morphology and composition of the products. X-ray photoelectron spectroscopy (XPS) measurements were conducted using an AXIS-SUPRA instrument from KRATOS. The surface morphology of the materials was examined using a JEM-2100 (200 KV) transmission electron microscope (JEOL, Tokyo, Japan), as well as to determine crystallographic information like lattice spacing and plane orientation. The overall surface area and pore size distribution patterns of the synthetic materials were analyzed by the specific surface area analyzer of ASAP 2420, in conjunction with the Brunauer–Emmett–Taylor (BET) method.

2.3. Electrode Preparation and Electrochemistry

The active material powder of LMFP, conductive carbon (C45), and polyvinylidene fluoride binder were mixed in N-methyl-2-pyrrolidone with a mass ratio of 93:3:4. Following comprehensive mixing, the resultant slurry was uniformly applied onto an aluminum substrate and subsequently dried under vacuum conditions at 120 °C for a duration of 10 h for subsequent application. The fabricated electrodes were sectioned into disks with a 12 mm diameter. The cells were assembled in an argon-filled glove box (O₂ and H₂O below 0.1 ppm), and the Celgard-2400 separator and a 1 mol/L LiPF₆ electrolyte solution (EC+DMC) were employed within the cells. The Li/LMFP half-cells underwent galvanostatic charge–discharge cycling within a voltage range of 2.0 to 4.5 V at a C-rate of 0.1 C (where 1 C equals 170 mA/g). Discharge rate experiments were conducted from 2.0 to 4.5 V at varying rates of 0.1, 0.2, 1, 2, 5, and 10 C. Longevity cycling tests, consisting of 1 C charge–discharge cycles within a 2–4.5 V range, were executed to assess the battery's lifespan. Electrochemical analyses of the coin cells were performed using a Wuhan LAND CT-2001A testing system. Furthermore, AC impedance spectroscopy of the coin cells was conducted with a Zahner Zennium pro electrochemical workstation to derive electrochemical parameters during the charge–discharge cycles, employing a test frequency spectrum of 10^{−2} to 10⁵ Hz and an imposed sinusoidal voltage perturbation of 10 mV.

3. Results and Discussion

Figure 2a exhibits the XRD spectra of LMFP-M1, LMFP-400, LMFP-450, LMFP-500, and LMFP-550. The XRD patterns exhibit a perfect alignment of the characteristic peaks and are devoid of any impurity peaks for the samples of LMFP-M1, LMFP-400, LMFP-450, LMFP-500, and LMFP-550. These patterns can be indexed to the Li(Mn, Fe)PO₄ structure, which is orthorhombic olivine (No. 89–7115), as opposed to the Pmnb (62) space group [30]. The elevation in initial sintering temperature does not cause notable changes in the diffraction peaks, suggesting that secondary crystallization can yield pure phase Li(Mn, Fe)PO₄ at 400–550 °C.

Figure 2b–f illustrate the nitrogen adsorption–desorption isotherms for LMFP-M1, LMFP-400, LMFP-450, LMFP-500, and LMFP-550. The obvious trend is that high temperature leads to an increased average diameter of crystalline particles and a consequent decrease in the specific surface area. As shown in Figure 2b, the specific surface area of the LMFP-M1 is about 33.1 m²/g (Table 1). After sintering at various temperatures, the specific surface areas were found to be 29.4 m²/g for LMFP-400 (Figure 2c), 25.6 m²/g for

LMFP-450 (Figure 2d), 25 m²/g for LMFP-500 (Figure 2e), and 22.4 m²/g for LMFP-550 (Figure 2f). The reason for this can be attributed to that without a carbon coating, high temperature will cause recrystallization, and the transformation of nanoplate edges to spherical shape, leads to as high as a 32% reduction in specific surface area. Combined with the subsequent SEM data, we concluded that secondary crystallization effectively reduces the specific surface area.

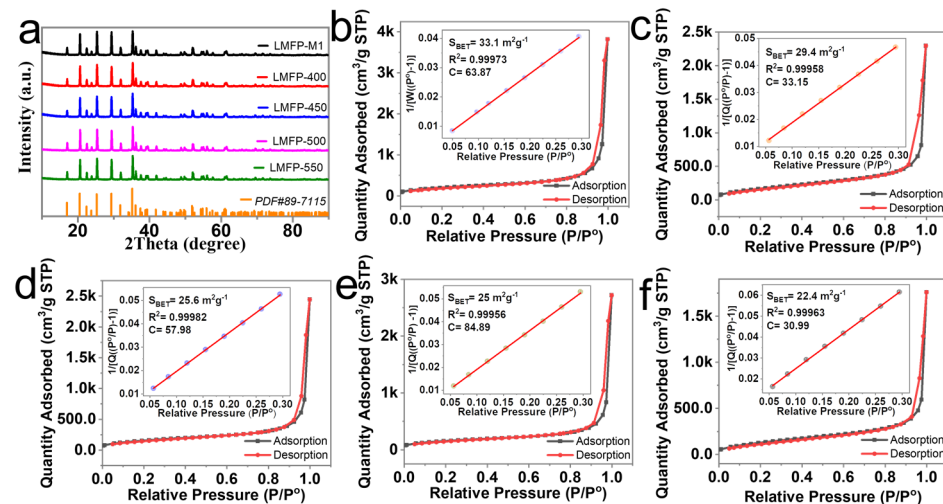


Figure 2. (a) XRD patterns and (b–f) Specific surface area of LMFP-M1 and LMFP-400, LMFP-450, LMFP-500, LMFP-550.

Table 1. The specific surface area of LMFP-M1 and LMFP-400, LMFP-450, LMFP-500, LMFP-550 samples, and the compaction density and discharge median voltage of the above samples after carbon coating.

Samples	LMFP-M1	LMFP-400	LMFP-450	LMFP-500	LMFP-550	
Specific surface area (m ² /g)	33.1	29.4	25.6	25.0	22.4	
After carbon coating	LMFP-M1/C	LMFP-400/C	LMFP-450/C	LMFP-500/C	LMFP-550/C	
Compaction density (g/cm ³)	1.96	2.18	2.27	2.34	2.43	
	0.1 C	4.028	4.025	3.996	4.009	3.995
	0.2 C	4.007	3.983	3.876	3.919	3.823
Median Voltage (V)	1 C	3.831	3.695	3.534	3.523	3.486
	2 C	3.518	3.469	3.379	3.361	3.330
	5 C	3.290	3.185	3.123	3.069	3.074
	10 C	3.009	2.771	2.754	2.660	2.712

Figure 3 displays the XPS spectra of LMFP-M1 and LMFP-500 by comparing the Fe2p_{3/2} spin-orbit splitting components; they are precisely aligned with the double peaks of LiFePO₄ [42,43]. The peak at 641.8 eV, corresponding to Mn2p_{3/2} spin-orbit splitting component, completely conforms to the double peaks of LiMnPO₄ [44,45]. The findings suggest that the binding energies of Fe and Mn remain unchanged after the secondary crystallization, implying that there is no impact on the valence states of the elements in LMFP-M1, thereby assuring structural integrity and electrochemical reversibility.

Figure 4a displays the SEM image of the LMFP-M1 by the solvothermal method. It can be found that most of the crystal particles of LMFP-M1 display well-dispersed morphology and flake-like crystals 80 nm in length and 20 nm in thickness (Figure S3a). Figure 4b and 4e show the SEM images of the LMFP-400, LMFP-450, LMFP-500, and LMFP-550 with the increase in primary calcination temperature (400–550 °C). The particle sizes of the secondary crystalline gradually increase, and their shape transforms from flake-like to spheroidal shape. In contrast, Figure 4b illustrates that LMFP-400 exhibits minimal alterations in size and shape. They retain the flake-like or rod-shaped structure, indicating

that the calcination temperature does not reach the material's melting point. LMFP-450 material particles calcined at 450 °C are significantly improved, as shown in Figure 4c, LMFP-450 particles transform from flake-like or rod-shaped to more spheroidal shape with smoother edges, and most crystal particles are around 100 nm without agglomeration, indicating that increased calcination temperature can promote melting, crystallization, and growth of crystal particles. When the calcination temperature is raised to 500 and 550 °C, the particle sizes of LMFP-500 and LMFP-550, as shown in Figure 4d,e, are noticeably increased. They exhibit rounder particle edges, and primary crystal particles are approximately 150–200 nm in length (Figure S3b), with agglomeration not being observed between the particles. The results indicate that the calcination temperature directly affects crystal growth during the primary calcination process. By controlling the sintering temperature and freeze-drying treatment, spheroidal particles of various sizes can be synthesized for enhancing powder compaction density. In contrast, Figure 4f displays the SEM image of the LMFP sample calcined at 550 °C without freeze-drying treatment, where the significant particle agglomeration is observed (Figure 1d). This indicates that particle fusion during calcination results in extended lithium ion transport paths and decreased electrochemical activity. Freeze-drying technique can produce a uniformly dispersed porous structure, effectively controlling particle growth during the secondary crystalline melting and crystallization process, thus preventing local agglomeration. Consequently, our methods were able to prepare the monodispersed single-crystal particles with a uniform size distribution. Figure S1 shows the SEM images of LMFP-M1/C, LMFP-400/C, LMFP-450/C, LMFP-500/C, and LMFP-550/C samples, which were treated by carbon coating. In contrast to Figure 1, the results reveal that secondary calcination primarily entails sucrose decomposition and carbonization, where carbon coating inhibits the growth of nanoparticles, leading to a small significant change in particle shape and size before and after calcination. Figure 4g–i present the EDS mapping spectra of the LMFP-500 sample. The result reveals a uniform distribution of Fe, Co, and Mn elements on the crystalline particles' surface. Despite secondary crystallization changing the particles' morphology and size, the distribution of metal elements remains unaffected. According to Table 1, the compaction densities of LMFP-M1/C, LMFP-400/C, LMFP-450/C, LMFP-500/C, and LMFP-550/C samples are 1.96, 2.18, 2.27, 2.34, and 2.43 g/cm³, respectively. The spheroidization of these sample particles reduces the interparticle gaps, and the increase in particle size ultimately leads to a significant enhancement of the material's compaction density, with a maximum increase of 24%, approaching the compaction density of commercial LFP. These changes contribute to enhancing the volumetric energy density of LiMn_{1-y}Fe_yPO₄ batteries.

Figure 5 presents the TEM images of LMFP-M1, LMFP-400, LMFP-450, LMFP-500 and LMFP-550. The particles of LMFP-M1 exhibits a cubic plate-shaped morphology with regular edges and distinct corners. The vertically aligned plate-like structure reveals that the nanosheets have a thickness of approximately 20 nm (Figure 5a). After carbon coating, the LMFP-M1/C sample exhibits a thin and uniform carbon cladding with a thickness of approximately 2–3 nm (Figure S2), and the carbon content is about 2 wt% of the total. As can be seen, the particles of LMFP-400, LMFP-450, LMFP-500, and LMFP-550 show an increase in particle size, smoother edges, and gradually blurred corners as the calcination temperature rises. The plate-like particles transform into an almost spherical shape, resulting in tighter contact between particles and fewer gaps. This enhances the material's compaction density, which is consistent with the SEM results in Figure 4. High-resolution transmission electron microscopy (TEM) images elucidate an increase in crystal particle size and a concurrent decrease in specific surface area, indicating that quasi-spherical single crystals do not possess a uniform crystallographic orientation. Moreover, TEM images in conjunction with the accompanying electron diffraction patterns confirm the pronounced single-crystallinity of the nanosheets. The observable lattice fringes and the related electron diffraction patterns of the LMFP nanosheets display a rectangular arrangement, validating the orthorhombic crystalline structure. The lattice spacing of 0.35 nm depicted in Figure 5b aligns with the (201) crystallographic planes of LMFP, suggesting a notable exposure of

the (010) facet [30]. In Figure 4d, the observed lattice spacings of 0.43 nm and 0.31 nm are associated with the (101) and (020) crystal planes, respectively. The 0.40 nm spacing presented in Figure 4f corresponds to the (210) planes. Furthermore, Figure 5h,k illustrate spacings of 0.35 nm and 0.52 nm, which are attributed to the (201) and (200) planes, respectively. In Figure 4j, the 0.43 nm spacing is indicative of the (101) planes [46,47]. The random orientation along the *b*-axis increases the diffusion path of lithium ions, leading to decreased electronic and ionic conductivity and increased polarization. Therefore, a balance must be found between compaction density and electrical conductivity, aiming to enhance the material's compaction density while maintaining its electrochemical performance as much as possible.

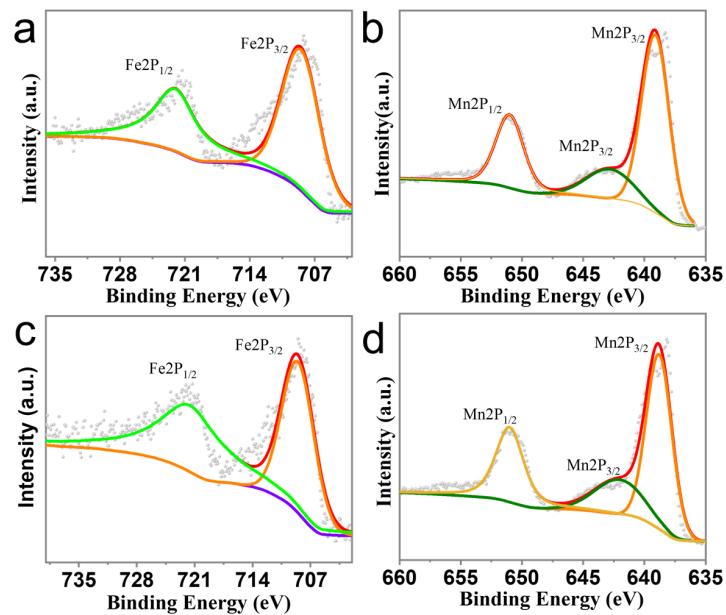


Figure 3. XPS images of LMFP-M1 (a,b), LMFP-500 (c,d).

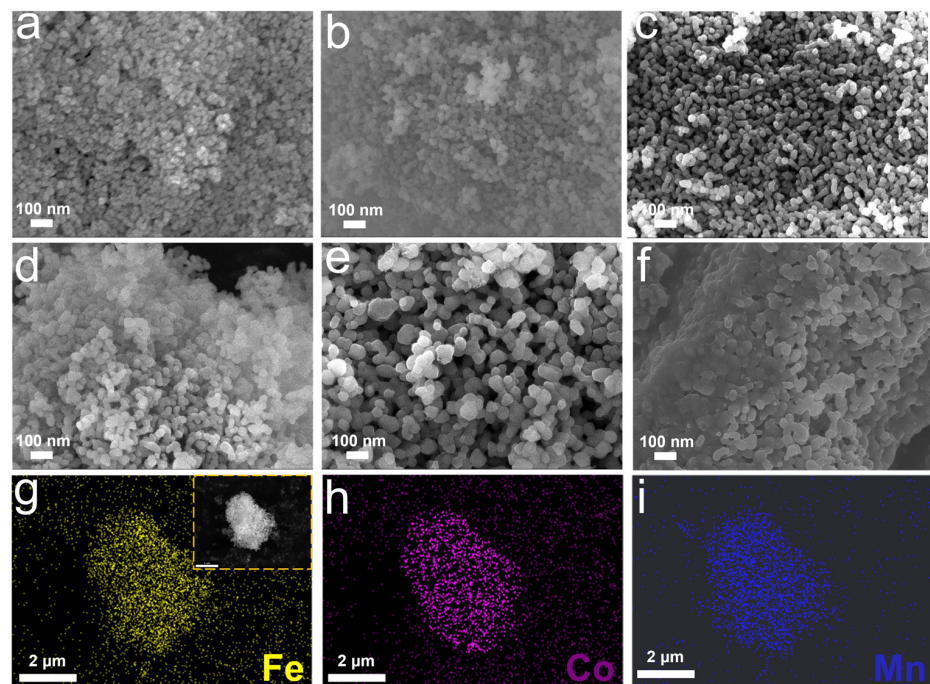


Figure 4. SEM images of LMFP-M1 (a), LMFP-400, LMFP-450, LMFP-500 and LMFP-550 (b–e); (f) EDS mapping of (g) Fe, (h) Co, and (i) Mn elements in LMFP-500 particle.

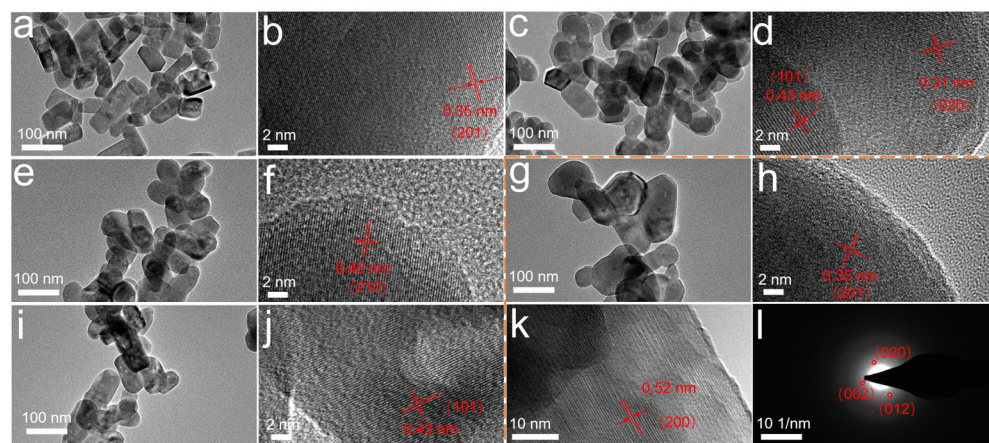


Figure 5. TEM images of LMFP-M1 (a,b) and LMFP-400 (c,d), LMFP-450 (e,f), LMFP-500 (g,h,k,l), LMFP-550 (i,j).

Figure 6 displays the rate discharge performance curves of LMFP-M1/C and the discharge capacities of the samples of LMFP-400/C, LMFP-450/C, LMFP-500/C, and LMFP-550/C at various current densities. All tests were conducted at 25 °C with a voltage range from 2.0 to 4.5 V. At a 0.1 C rate, the specific capacities of LMFP-M1/C, LMFP-400/C, LMFP-450/C, LMFP-500/C, and LMFP-550/C are 164.0, 164.2, 165.0, 166.2, and 162.2 mAh/g, respectively (Figure 6a). This suggests that the specific capacity remains stable despite the increase in material compaction density. Particularly, LMFP-500/C has a compaction density of 2.34 g/cm³, which exhibits the highest specific capacity. As shown in Figure 6b, the discharge capacities of LMFP-M1/C, LMFP-400/C, LMFP-450/C, LMFP-500/C, and LMFP-550/C at the rate of 0.1, 0.2, 1, 2, 5, and 10 C were measured. Specifically, the discharge capacities of LMFP-M1/C are 164.0, 162.9, 151.8, 148.1, 143.6, and 136.1 mAh/g, LMFP-400/C are 164.2, 154.2, 146.5, 143.3, 134.6, and 116.1 mAh/g, LMFP-450/C are 165.0, 153.7, 142.3, 137.3, 126.7, and 107.2 mAh/g, LMFP-500/C are 166.2, 151.6, 139.5, 133.8, 122.2, and 103.5 mAh/g, and LMFP-550/C are 162.2, 145.7, 131.0, 125.6, 117.6, and 105.4 mAh/g, respectively (Table S2). LMFP-500/C shows good capacity retention among all rates, its compaction density increases from 2.18 to 2.34 g/cm³, marking a 7.3% growth. After secondary crystallization, the particles develop a quasi-spherical structure, resulting in an increased *b*-axis and a longer lithium ion transport path, thereby slightly reducing the specific capacity. Nevertheless, samples prepared at temperatures below 500 °C maintain favorable electrochemical performance. While further increasing the temperature can improve the material's compaction density, it leads to a more pronounced decline in electrochemical performance. Table 1 displays the median discharge voltages of LMFP-M1/C, LMFP-400/C, LMFP-450/C, LMFP-500/C, and LMFP-550/C samples at different current densities. At rates of 0.1, 0.2, 1, 2, 5, and 10 C, the voltages of LMFP-400/C are 4.025, 3.983, 3.695, 3.469, 3.185, and 2.771 V, respectively; those of LMFP-500/C are 4.009, 3.919, 3.523, 3.361, 3.069, and 2.660 V. At various rates, materials with different compaction densities demonstrate similar patterns in discharge voltage polarization. Even at a high rate of 10 C, LMFP-500/C exhibits just a 0.111 V decrease in median voltage, indicative of the excellent voltage retention capability. Figure 6c displays the cathode material energy densities of LMFP-M1/C and the secondary crystalline samples (LMFP-400/C, LMFP-450/C, LMFP-500/C, and LMFP-550/C). The figure demonstrates a positive correlation between the cathode electrode energy density and both the specific capacity and median voltage. Although the energy density of the materials with a high compaction density slightly decreases, the overall retention rate remains satisfactory. Figure 6d illustrates the cycle life curves of LMFP-M1/C, LMFP-400/C, LMFP-450/C, LMFP-500/C, and LMFP-550/C samples at 1 C. The sintering temperatures will gradually lead to the first capacity decay after 200 cycles, the trend of capacity decay is completely similar, indicating the unaffected cyclic stability of the materials. As seen in Figure 6e, full pouch cell electrochemical tests

using the high-compaction-density material LMFP-500/C show discharge capacities of 144.1, 143.8, and 142.6 mAh/g at 0.5, 1, and 3 C, respectively, which demonstrate a superior high-rate performance, approaching a 99% retention rate at 3 C. This suggests that the monodispersed spherical particle structure effectively preserves the electrochemical properties of the LMFP-M1/C. After 800 cycles of 1 C charging and discharging, the capacity retention is 90% (Figure 6f), indicating a full cell lifespan exceeding 2500 cycles, consistent with power battery longevity standards. Hence, the LMFP-500/C sample demonstrates preferable electrochemical performance compared with materials prepared by various methods (Table S1).

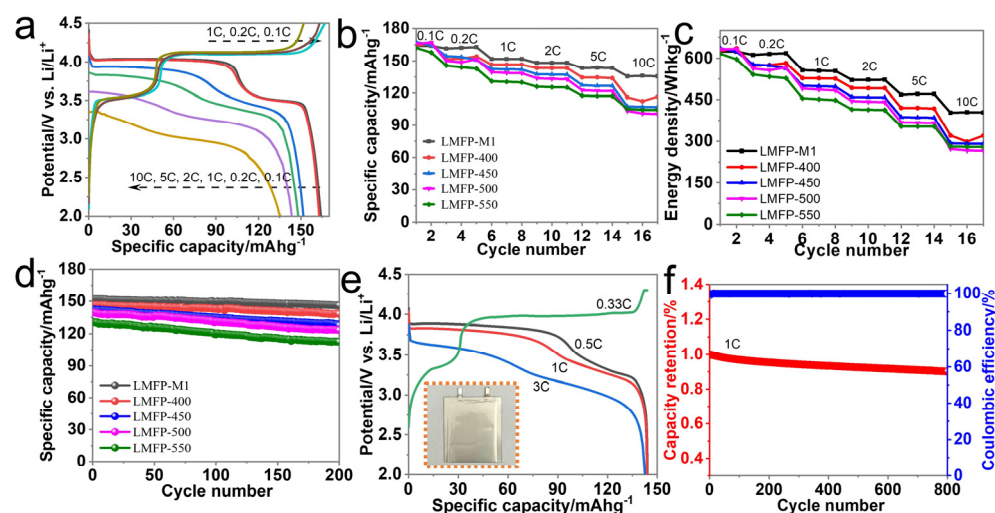


Figure 6. (a) Rate performance of LMFP-M1/C. (b) C-rate, (c) cathode material energy densities and (d) cycling performance of LMFP-M1/C and LMFP-400/C, LMFP-450/C, LMFP-500/C, LMFP-550/C. (e) C-rate and (f) cycling performance of LMFP-500/C pouch cell.

Figure 7a displays the cyclic voltammetry (CV) curves of all the samples. The CV curves are very similar, which display two pairs of asymmetric redox couples, specifically for $\text{Fe}^{2+}/\text{Fe}^{3+}$ (3.3/3.8 V) and $\text{Mn}^{2+}/\text{Mn}^{3+}$ (3.7/4.4 V) [48]. The redox peak voltage differences for the LMFP-M1/C sample are $\text{Fe}^{2+}/\text{Fe}^{3+}$ at 0.450 V and $\text{Mn}^{2+}/\text{Mn}^{3+}$ at 0.697 V; LMFP-400/C at 0.451 and 0.700 V; LMFP-450/C at 0.463 and 0.700 V; LMFP-500/C at 0.518 and 0.772 V; and LMFP-550/C at 0.506 and 0.791 V, respectively. The CV analysis indicates that the LMFP-M1/C material has the smallest redox peak voltage difference, along with the largest peak current and redox peak area. An incremental rise in the voltage difference in the redox peaks is noted concomitantly with an increase in compaction density. The size and morphology of particles are influential factors in the kinetics of lithium ion intercalation and deintercalation processes. In comparison to LMFP-400/C, the high compaction density sample LMFP-500/C exhibits increases in the redox peak voltage difference of 0.067 and 0.091 V, respectively. This relatively minor difference leads to a limited impact on the kinetic properties. Figure 7b shows the electrochemical impedance spectroscopy (EIS) spectra of LMFP-M1/C and the LMFP-400/C, LMFP-450/C, LMFP-500/C, and LMFP-550/C samples. The results illustrate that the charge transfer resistance (R_{ct}) of the LMFP-M1/C sample is 67.1 Ω , while the R_{ct} of LMFP-400/C, LMFP-450/C, LMFP-500/C, and LMFP-550/C is 76.4, 76.7, 77.2, and 86.8 Ω , respectively [49]. This suggests that the charge transfer resistances of the materials remain stable even with an increase in compaction density, showing no significant change, and the kinetic properties of the high compaction density material remain largely unaffected. The sloping lines in the graph represent the diffusion impedance of lithium ions within the material's lattice, consistent with the trend in R_{ct} . Freeze-drying treatment prevents particle agglomeration during secondary sintering, thereby maintaining good monodispersity. However, the particle size will still increase relative to the initial

precursor, resulting in increased lithium ion transport distance and diffusion impedance within the crystal.

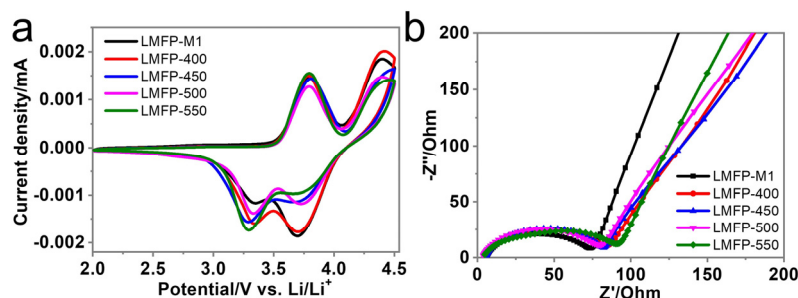


Figure 7. (a) CV curves and (b) fitted Nyquist plots of LMFP-M1/C and LMFP-400/C, LMFP-450/C, LMFP-500/C, LMFP-550/C.

4. Conclusions

The development of $\text{LiMn}_{0.69}\text{Co}_{0.01}\text{Fe}_{0.3}\text{PO}_4$ (LMFP) cathode materials via freeze-drying-assisted secondary crystallization marks a significant advancement in lithium ion battery technology. Our method can enhance compaction density and electrochemical performance, offering a promising pathway to higher energy density and improved cycling stability in lithium ion batteries. These improvements are crucial for applications in electric vehicles and renewable energy storage systems. Future research directions include optimizing this technique for a broader range of cathode materials, potentially revolutionizing the efficiency and reliability of next-generation lithium ion batteries.

Supplementary Materials: The following supporting information can be downloaded at: <https://www.mdpi.com/article/10.3390/batteries10040114/s1>, Figure S1: SEM images of LMFP-M1/C (a) and LMFP-400/C, LMFP-450/C, LMFP-500/C, and LMFP-550/C (b–e); Figure S2: The TEM image of LMFP-M1/C; Figure S3: particle size distribution of (a) LMFP-M1 and (b) LMFP-500; Table S1: Cycle performance comparison of LMFP-based cathode materials prepared by different methods; Table S2: The specific capacities at various C-rates of LMFP-M1/C, LMFP-400/C, LMFP-450/C, LMFP-500/C, and LMFP-550/C. References [27,36,45,50–55] are cited in the Supplementary Materials.

Author Contributions: Conceptualization, C.S. and Y.X.; methodology, S.L.; software, H.L.; validation, H.Z. and H.H.; formal analysis, S.L.; investigation, Y.X.; resources, C.S.; data curation, J.Z.; writing—original draft preparation, S.L.; writing—review and editing, C.S.; visualization, B.A.; supervision, L.L.; project administration, H.Z.; funding acquisition, C.S. All authors have read and agreed to the published version of the manuscript.

Funding: Acknowledgment is extended to the National Natural Science Foundation of China for their support (No. 11972178, 51972156, U1904190, 52272243, and 22202065), the Natural Science Foundation for Excellent Young Scholars of Henan Province (Grant No. 212300410091), and the Program for Science and Technology Innovation Talents in Universities of Henan Province (No. 22HASTIT005).

Data Availability Statement: The data presented in this study are available in Supplementary Materials.

Conflicts of Interest: The authors declare no conflicts of interest.

References

- Liu, J.; Wu, Y.; Zhang, B.; Xiao, X.; Hu, Q.; Han, Q.; Wang, L.; Bei, F.; He, X. A Promising Solid-state Synthesis of $\text{LiMn}_{1-y}\text{Fe}_y\text{PO}_4$ Cathode for Lithium-ion Batteries. *Small* **2023**, e2309629. [CrossRef]
- Renier, O.; Pellini, A.; Spooen, J. Advances in the Separation of Graphite from Lithium Iron Phosphate from End-of-Life Batteries Shredded Fine Fraction Using Simple Froth Flotation. *Batteries* **2023**, *9*, 589. [CrossRef]
- Padhi, A.K.; Nanjundaswamy, K.S.; Goodenough, J.B. Phospho-olivines as Positive-electrode Materials for Rechargeable Lithium Batteries. *J. Electrochem. Soc.* **1997**, *144*, 1188. [CrossRef]

4. Malik, R.; Abdellahi, A.; Ceder, G. A Critical Review of the Li Insertion Mechanisms in LiFePO₄ Electrodes. *J. Electrochem. Soc.* **2013**, *160*, A3179. [[CrossRef](#)]
5. Wang, J.; Sun, X. Olivine LiFePO₄: The Remaining Challenges for Future Energy Storage. *Energy Environ. Sci.* **2015**, *8*, 1110–1138. [[CrossRef](#)]
6. Chen, Y.; Chen, L.; Jiang, L.; Zhu, X.; Li, F.; Liu, X.; Mai, K.; Zhang, Z.; Fan, X.; Lv, X. Multifunctional Radical Polymers-enabled Rapid Charge/Discharge and High Capacity for Flexible Self-standing LiFePO₄/PETM/SWNT Hybrid Electrodes. *Chem. Eng. J.* **2024**, *482*, 149008. [[CrossRef](#)]
7. Chung, S.-Y.; Bloking, J.T.; Chiang, Y.-M. On the Electronic Conductivity of Phospho-olivines as Lithium Storage Electrodes. *Nat. Mater.* **2003**, *2*, 702–703. [[CrossRef](#)]
8. Yang, Z.; Dai, Y.; Wang, S.; Yu, J. How to Make Lithium Iron Phosphate Better: A Review Exploring Classical Modification Approaches In-depth and Proposing Future Optimization Methods. *J. Mater. Chem. A* **2016**, *4*, 18210–18222. [[CrossRef](#)]
9. Nwachukwu, I.M.; Nwanya, A.C.; Ekwealor AB, C.; Ezema, F. Research Progress in Solid-state Synthesized LiMnPO₄ Cathode Material for Li-ion Battery Applications. *Appl. Surf. Sci. Adv.* **2023**, *18*, 100505. [[CrossRef](#)]
10. Chen, Z.; Wang, W.; Duan, J.; Qian, F.; Cao, Y.; He, J.; Wang, D.; Dong, P.; Zhang, J. Highly Efficient Synthesis of Nano LiMn_{0.90}Fe_{0.10}PO₄/C Composite via Mechanochemical Activation Assisted Calcination. *Ceram. Int.* **2023**, *49*, 18483–18490.
11. Zhou, F.; Kang, K.; Maxisch, T.; Ceder, G.; Morgan, D. The Electronic Structure and Band Gap of LiFePO₄ and LiMnPO₄. *Solid State Commun.* **2004**, *132*, 181–186. [[CrossRef](#)]
12. Aravindan, V.; Gnanaraj, J.; Lee, Y.-S.; Madhavi, S. LiMnPO₄—A next Generation Cathode Material for Lithium-ion Batteries. *J. Mater. Chem. A* **2013**, *1*, 3518–3539. [[CrossRef](#)]
13. Lee, H.; Park, J.; Kim, M.; Choi, K.; Kim, K.; Im, D. High-Energy-Density Li-O₂ Battery at Cell Scale with Folded Cell Structure. *Joule* **2018**, *11*, 016. [[CrossRef](#)]
14. Shi, C.; Takeuchi, S.; Alexander, G.; Hamann, T.; O'Neill, J.; Dura, J.; Wachsman, E. High Sulfur Loading and Capacity Retention in Bilayer Garnet Sulfurized-Polyacrylonitrile/Lithium-Metal Batteries with Gel Polymer Electrolytes. *Adv. Energy Mater.* **2023**, *13*, 2301656. [[CrossRef](#)]
15. Shi, C.; Hamann, T.; Takeuchi, S.; Alexander, G.; Nolan, A.; Limpert, M.; Fu, Z.; O'Neill, J.; Godbey, G.; Dura, J.; et al. 3D Asymmetric Bilayer Garnet-Hybridized High-Energy-Density Lithium-Sulfur Batteries. *ACS Appl. Mater. Interfaces* **2023**, *15*, 751–760. [[CrossRef](#)]
16. Lu, X.; He, H.; Qiu, H.; Jiang, W.; Zhang, Y.; He, W. Ethylene Glycol Solvothermal Synthesis of LiMnPO₄ Nanoparticles with High (200) Crystal Face Exposure for High Performance Lithium-ion Batteries. *Mater. Sci. Eng. B* **2024**, *299*, 117032. [[CrossRef](#)]
17. Dong, Y.; Xie, H.; Song, J.; Xu, M.; Zhao, Y.; Goodenough, J. The Prepared and Electrochemical Property of Mg Doped LiMnPO₄ Nanoplates as Cathode Materials for Lithium-ion Batteries. *J. Electrochem. Soc.* **2012**, *159*, A995. [[CrossRef](#)]
18. Yonemura, M.; Yamada, A.; Takei, Y.; Sonoyama, N.; Kanno, R. Comparative Kinetic Study of Olivine Li_xMPO₄ (M = Fe, Mn). *J. Electrochem. Soc.* **2004**, *151*, A1352. [[CrossRef](#)]
19. Nishimura, S.-I.; Kobayashi, G.; Ohoyama, K.; Kanno, R.; Yashima, M.; Yamada, A. Experimental Visualization of Lithium Diffusion in Li_xFePO₄. *Nat. Mater.* **2008**, *7*, 707–711. [[CrossRef](#)] [[PubMed](#)]
20. Yamada, A.; Kudo, Y.; Liu, K.-Y. Phase Diagram of Li_x(Mn_yFe_{1-y})PO₄ (0 ≤ x, y ≤ 1). *J. Electrochem. Soc.* **2001**, *148*, A1153. [[CrossRef](#)]
21. Yamada, A.; Chung, S. Crystal Chemistry of the Olivine-Type Li(Mn_yFe_{1-y})PO₄ and (Mn_yFe_{1-y})PO₄ as Possible 4 V Cathode Materials for Lithium Batteries. *J. Electrochem. Soc.* **2001**, *148*, A960–A967. [[CrossRef](#)]
22. Dong, Y.; Wang, L.; Zhang, S.; Zhao, Y.; Zhou, J.; Xie, H.; Goodenough, J. Two-phase Interface in LiMnPO₄ Nanoplates. *J. Power Sources* **2012**, *215*, 116–121. [[CrossRef](#)]
23. Zhu, K.; Zhang, W.; Du, J.; Liu, X.; Tian, J.; Ma, H.; Liu, S.; Shan, Z. Reaction Mechanism and Influence of the Experimental Variables for Solvothermal Synthesized LiMnPO₄ Nanoplates. *J. Power Sources* **2015**, *300*, 139–146. [[CrossRef](#)]
24. Esmezjan, L.; Mikhailova, D.; Etter, M.; Cabana, J.; Grey, C.; Indris, S.; Ehrenberg, H. Electrochemical Lithium Extraction and Insertion Process of Sol-gel Synthesized LiMnPO₄ via Two-Phase Mechanism. *J. Electrochem. Soc.* **2019**, *166*, A1257–A1265. [[CrossRef](#)]
25. Yamada, A.; Kudo, Y.; Liu, K.Y. Reaction Mechanism of the Olivine-type Li_xMn_{0.6}Fe_{0.4}PO₄ (0 < x < 1). *J. Electrochem. Soc.* **2001**, *148*, A747–A754.
26. Huang, W.; Tao, S.; Zhou, J.; Si, C.; Chen, X.; Huang, W.; Jin, C.; Chu, W.; Song, L.; Wu, Z. Phase Separations in LiFe_{1-x}Mn_xPO₄: A Random Stack Model for Efficient Cathode Materials. *J. Phys. Chem. C* **2013**, *118*, 796–803. [[CrossRef](#)]
27. Lei, Z.; Naveed, A.; Lei, J.; Wang, J.; Yang, J.; Nuli, Y.; Meng, X.; Zhao, Y. High performance nano-sized LiMn_{1-x}Fe_xPO₄ cathode materials for advanced lithium-ion batteries. *RSC Adv.* **2017**, *7*, 43708–43715. [[CrossRef](#)]
28. Malik, R.; Zhou, F.; Ceder, G. Phase Diagram and Electrochemical Properties of Mixed Olivines from First-principles Calculations. *Phys. Rev. B* **2009**, *79*, 214201. [[CrossRef](#)]
29. Dimesso, L.; Förster, C.; Jaegermann, W.; Khanderi, J.; Tempel, H.; Popp, A.; Engstler, J.; Schneider, J.; Sarapulova, A.; Mikhailova, D.; et al. Developments in Nanostructured LiMPO₄ (M = Fe, Co, Ni, Mn) Composites Based on Three Dimensional Carbon Architecture. *Chem. Soc. Rev.* **2012**, *41*, 5068–5080. [[CrossRef](#)] [[PubMed](#)]
30. Yang, L.; Deng, W.; Xu, W.; Tian, Y.; Wang, A.; Wang, B.; Zou, G.; Hou, H.; Deng, W.; Ji, X. Olivine LiMn_xFe_{1-x}PO₄ Cathode Materials for Lithium Ion Batteries: Restricted Factors of Rate Performances. *J. Mater. Chem. A* **2021**, *9*, 14214–14232. [[CrossRef](#)]

31. Huang, S.; Lin, W.; Li, L.; Liu, P.; Huang, T.; Huang, Z.; Kong, J.; Xiong, W.; Yu, W.; Ye, S.; et al. Pathway for High-energy Density LiMnFePO₄ Cathodes. *Prog. Nat. Sci. Mater. Int.* **2023**, *33*, 126–131. [[CrossRef](#)]
32. Li, Y.; Xu, G.; Fan, S.M.; Ma, J.; Shi, X.; Long, Z.; Deng, W.; Fan, W.; Yang, S. Synthesis of Carbon-coated LiMn_{0.8}Fe_{0.2}PO₄ Materials via an Aqueous Rheological Phase-assisted Solid-state Method. *J. Solid State Electrochem.* **2020**, *24*, 821–828. [[CrossRef](#)]
33. Liu, S.; Zheng, J.; Zhang, B.; Wu, Y.; Liu, J.; Yin, L.; Zhan, M.; Xiao, Y.; An, B.; Wang, L.; et al. Engineering Manganese-rich Phospho-olivine Cathode Materials with Exposed Crystal {010} Facets for Practical Li-ion Batteries. *Chem. Eng. J.* **2023**, *454*, 139986. [[CrossRef](#)]
34. Jin, Y.; Tang, X.; Wang, Y.; Dang, W.; Huang, J.; Fang, X. High-tap Density LiFePO₄ Microsphere Developed by Combined Computational and Experimental Approaches. *CrystEngComm* **2018**, *20*, 6695–6703. [[CrossRef](#)]
35. Yang, S.; Ma, R.; Hu, M.; Xi, L.; Lu, Z.; Chung, C. Solvothermal Synthesis of Nano-LiMnPO₄ from Li₃PO₄ Rod-like Precursor: Reaction Mechanism and Electrochemical Properties. *J. Mater. Chem.* **2012**, *22*, 25402–25408. [[CrossRef](#)]
36. Zhang, X.; Hou, M.; Tamirate, A.G.; Zhu, H.; Wang, C.; Xia, Y. Carbon Coated Nano-sized LiMn_{0.8}Fe_{0.2}PO₄ Porous Microsphere Cathode Material for Li-ion Batteries. *J. Power Sources* **2020**, *448*, 227438. [[CrossRef](#)]
37. Liu, H.; Liu, Y.; An, L.; Zhao, X.; Wang, L.; Liang, G. High Energy Density LiFePO₄/C Cathode Material Synthesized by Wet Ball Milling Combined with Spray Drying Method. *J. Electrochem. Soc.* **2017**, *164*, A3666. [[CrossRef](#)]
38. Wang, X.; Wen, L.; Zheng, Y.; Liu, H.; Liang, G. Facile Synthesis and Electrochemical Properties of High Tap Density LiFePO₄/C. *Ionics* **2019**, *25*, 4589–4596. [[CrossRef](#)]
39. Li, Y.; Wang, L.; Zhang, H.; Liang, F.; Yao, Y.; Zhang, K. Freeze Drying under Vacuum Assisted Synthesis of LiFePO₄@MWCNTs Composite with Phytic acid as Phosphorus Source for Advanced Li-storage. *Vacuum* **2021**, *193*, 110541. [[CrossRef](#)]
40. Zhecheva, E.; Mladenov, M.; Zlatilova, P.; Koleva, V.; Stoyanova, R. Particle Size Distribution and Electrochemical Properties of LiFePO₄ Prepared by a Freeze-drying Method. *J. Phys. Chem. Solids* **2010**, *71*, 848–853. [[CrossRef](#)]
41. Palomares, V.; Goñi, A.; de Muro, L.G.; de Meatza, I.; Bengoechea, M.; Miguel, O.; Rojo, T. New Freeze-drying Method for LiFePO₄ synthesis. *J. Power Sources* **2007**, *171*, 879–885. [[CrossRef](#)]
42. Hadouchi, M.; Yaqoob, N.; Kaghazchi, P.; Tang, M.; Liu, J.; Sang, P.; Fu, Y.; Huang, Y.; Ma, J. Fast Sodium Intercalation in Na₂FeV(PO)₄, A Novel Sodium-Deficient NASICON Cathode for Sodium-ion Batteries. *Energy Storage Mater.* **2021**, *35*, 192–202. [[CrossRef](#)]
43. Hou, J.; Hadouchi, M.; Sui, L.; Liu, J.; Tang, M.; Kan, W.; Avdeev, M.; Zhong, G.; Liao, Y.; Lai, Y.; et al. Unlocking Fast and Reversible Sodium Intercalation in NASICON Na₄MnV(PO)₃ by Fluorine Substitution. *Energy Storage Mater.* **2021**, *42*, 307–316. [[CrossRef](#)]
44. Su, J.; Wei, B.Q.; Rong, J.; Yin, W.; Ye, Z.; Tian, X.; Ren, L.; Cao, M.; Hu, C. A General Solution-chemistry Route to the Synthesis LiMPO₄ (M=Mn, Fe, and Co) Nanocrystals with [010] Orientation for Lithium ion Batteries. *J. Solid State Chem.* **2011**, *184*, 2909–2919. [[CrossRef](#)]
45. Liang, Y.; Chen, S.; Fan, C.L.; Yang, J.; Song, Z.; Zeng, X. High-performance LiMn_{0.8}Fe_{0.2}PO₄/C Cathode Prepared by Using the Toluene-soluble Component of Pitch as a Carbon Source. *Int. J. Energy Res.* **2021**, *45*, 19103–19119. [[CrossRef](#)]
46. Peng, L.; Zhang, X.; Fang, Z.; Zhu, Y.; Xie, Y.; Cha, J.; Yu, G. A General Facet-Controlled Synthesis of Single-Crystalline {010}-Oriented LiMPO₄ (M = Mn, Fe, Co) Nanosheets. *Chem. Mater.* **2017**, *29*, 10526–10533. [[CrossRef](#)]
47. Wang, Y.; Yu, F. Probing the Morphology Dependence, Size Preference and Electron/ion Conductance of Manganese-based Lithium Transition-metal Phosphate as Cathode Materials for High-performance Lithium-ion Battery. *J. Alloys Compd.* **2021**, *850*, 156773. [[CrossRef](#)]
48. Yang, H.; Fu, C.; Sun, Y.; Wang, L.; Liu, T. Fe-doped LiMnPO₄@C Nanofibers with High Li-ion Diffusion Coefficient. *Carbon* **2019**, *11*, 067. [[CrossRef](#)]
49. Mc Carthy, K.; Gullapalli, H.; Kennedy, T. Electrochemical Impedance Correlation Analysis for the Estimation of Li-ion Battery State of Charge, State of Health and Internal Temperature. *J. Energy Storage* **2022**, *50*, 104608. [[CrossRef](#)]
50. Chen, J.; Zhang, D.Y.; Qiao, J.; Chang, C. High Performance of LiMn_{1-x}Fe_xPO₄/C (0 ≤ x ≤ 0.5) Nanoparticles Synthesized by Microwave-Assisted Solvothermal Method. *Ionics* **2018**, *24*, 689–696. [[CrossRef](#)]
51. Deng, Z.; Wang, Q.; Peng, D.; Liu, H.; Chen, Y. Fast Precipitation-Induced LiFe_{0.5}Mn_{0.5}PO₄/C Nanorods with A Fine Size and Large Exposure of the (010) Faces for High-Performance Lithium-ion Batteries. *J. Alloys Compd.* **2019**, *794*, 178–185. [[CrossRef](#)]
52. Li, J.; Guo, C.; Qin, Y.; Ning, X. Ascorbic Acid-Assisted Solvothermal Synthesis of LiMn_{1-x}Fe_xPO₄/C Nanoparticles for High Performance Li-ion Cathode Materials. *Mater. Technol.* **2020**, *35*, 9–10. [[CrossRef](#)]
53. Lu, C.-H.; Subburaj, T.; Chiou, H.-T. Facile Sol-Gel Synthesis of LiMn_{0.5}Fe_{0.5}PO₄ Cathode Materials Fostered by Bio-Derived Natural Agar. *Ionics* **2020**, *26*, 1051–1056. [[CrossRef](#)]
54. Meng, Y.; Wang, Y.; Zhang, Z.; Chen, X.; Guo, Y.; Xiao, D. A Phytic Acid Derived LiMn_{0.5}Fe_{0.5}PO₄/Carbon Composite of High Energy Density for Lithium Rechargeable Batteries. *Sci. Rep.* **2019**, *9*, 6665. [[CrossRef](#)]
55. Wang, Y.; Wang, Y.; Liu, X.; Zhu, B.; Wang, F. Solvothermal Synthesis of LiFe_{1/3}Mn_{1/3}Co_{1/3}PO₄ Solid Solution as Lithium Storage Cathode Materials. *RSC Adv.* **2017**, *7*, 14354. [[CrossRef](#)]

Disclaimer/Publisher's Note: The statements, opinions and data contained in all publications are solely those of the individual author(s) and contributor(s) and not of MDPI and/or the editor(s). MDPI and/or the editor(s) disclaim responsibility for any injury to people or property resulting from any ideas, methods, instructions or products referred to in the content.